

See discussions, stats, and author profiles for this publication at: <https://www.researchgate.net/publication/51802772>

Interface Effects on the Magnetism of CoPt-Supported Nanostructures

ARTICLE *in* NANO LETTERS · NOVEMBER 2011

Impact Factor: 13.59 · DOI: 10.1021/nl203449y · Source: PubMed

CITATIONS

16

READS

30

5 AUTHORS, INCLUDING:



Giovanni Barcaro

Italian National Research Council

106 PUBLICATIONS 1,598 CITATIONS

SEE PROFILE



Fabio Ribeiro Negreiros

Universidade Federal do ABC (UFABC)

38 PUBLICATIONS 287 CITATIONS

SEE PROFILE



Riccardo Ferrando

Università degli Studi di Genova

234 PUBLICATIONS 8,376 CITATIONS

SEE PROFILE



Alessandro Fortunelli

Italian National Research Council

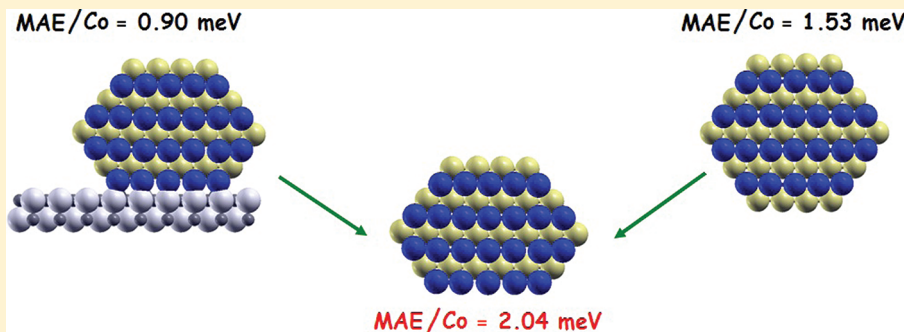
210 PUBLICATIONS 3,986 CITATIONS

SEE PROFILE

Interface Effects on the Magnetism of CoPt-Supported Nanostructures

Giovanni Barcaro,[†] Luca Sementa,[†] Fabio R. Negreiros,[†] Riccardo Ferrando,[‡] and Alessandro Fortunelli^{*,†}[†]CNR-IPCF, Istituto per i Processi Chimico-Fisici, Via G. Moruzzi 1, Pisa, I56124, Italy[‡]Physics Department, Via Dodecaneso 33, Genoa, I16146, Italy

ABSTRACT:



The magnetism of CoPt nanostructures supported on the MgO(100) surface is investigated via first-principles simulations using 1D models. Nanostructures with L1₀ chemical ordering and cube-on-cube epitaxy are predicted to possess large magnetic moments and easy magnetization axis perpendicular to the surface. However, their magnetic anisotropy energy is roughly halved with respect to the bulk alloy due to a peculiar mixing of particle and support electronic states. The general factors at play in determining this behavior and the implications of these findings are discussed in view of designing room-temperature magnetic bits.

KEYWORDS: Magnetic anisotropy energy, density functional theory, oxide supports, substrate effect, nanoparticles, nanowires

In the strive for the ultimate limit of miniaturization of memory bits, nanospintronics¹ represents a fascinating path. Magnetic nanostructures bearing a spin unit could be manipulated and exploited in ultrahigh-density recording devices.² Two requirements have so far hindered progress in this field: the magnetic anisotropy energy (MAE), that is, the energy barrier to the reorientation of the spin direction, should be large enough to overcome the superparamagnetic regime at room temperature, and for supported particles the easy magnetization axis should preferentially be perpendicular to the substrate surface.³ CoPt nanoparticles at 1:1 composition in the L1₀ ordered phase are promising candidates in this perspective, as the CoPt alloy exhibits among the largest known bulk MAE,² so that properly oriented CoPt particles of few thousands of atoms could effectively function as room-temperature memory bits. The environment (such as the support) used to orient the particles however plays a crucial role in determining their structural and electronic features;⁴ rigorous knowledge on this topic is available for the case of metal supports⁵ but basically lacking for the more interesting oxide ones. Here, we investigate at the first-principles level interfacial effects on the structural and magnetic properties of oxide-supported CoPt nanostructures. We show that L1₀-ordered nanostructures with easy magnetization axis perpendicular to the surface can indeed be stabilized on MgO(100), however, at the price of a substantial reduction of the MAE. From this analysis, the general factors at play in determining this behavior are singled out, providing a framework for the design of nanospintronics devices.

For a full understanding and control of the physics of metal/support interface, we focus on a model system: the single-crystal MgO(100) surface as the substrate of CoPt nanostructures. Oxide surfaces are commonly used for the growth of metal nanoparticles and nanoalloys, and the MgO(100) surface is one of the best characterized and is widely used in both model studies and applications.⁶ CoPt particles are interesting not only for magnetic⁷ but also for catalytic⁸ applications. The first issue to be faced when studying the magnetism of metal nanodots concerns the preferred particle structure. It is known in fact that peculiar structural phenomena can occur when reaching the nanoscale regime.⁹ In the present case, both experimental evidence for particles embedded in weakly interacting substrates such as amorphous carbon¹⁰ and theoretical simulations for free clusters¹¹ show that noncrystalline structures are favored for CoPt and FePt particles up to ~3–4 nm in diameter. Interface effects change the situation drastically; for CoPt mixed aggregates deposited on MgO(100), extensive simulations using many-body empirical potentials¹² (see also Methods section) indicate that a transition from noncrystalline (polyicosahedral) supported motifs to face-centered cubic (fcc)-like L1₀ configurations with cube-on-cube epitaxy is expected around 1:1 Co/Pt composition when the number of atoms exceeds roughly ~200. A further important structural information is that the

Received: October 3, 2011

Revised: November 14, 2011

Published: November 16, 2011

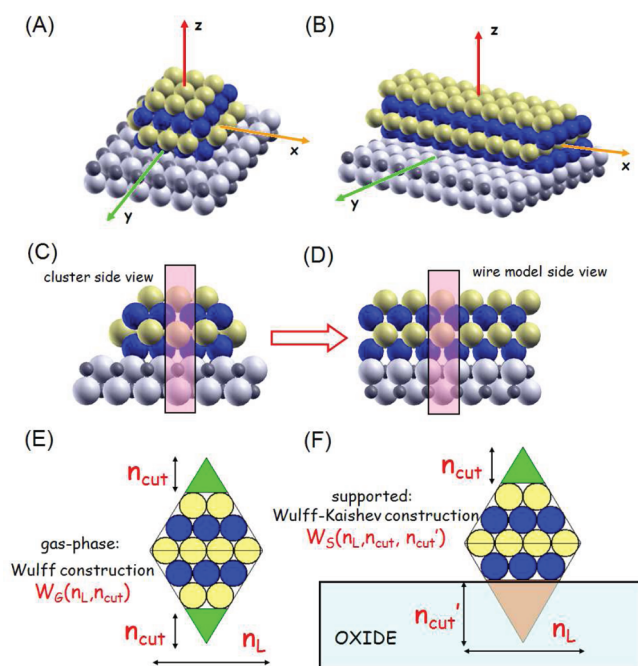


Figure 1. One-dimensional (wire) modeling of supported binary particles. A 0D particle (A) and a side view with its cross-section (C) are shown, together with a piece of the corresponding 1D wire model (B) and a side view with its cross-section (D). The Cartesian axes are also indicated in (A,B). Side views are along y -axis. The truncations of a free (E) and supported (F) wire viewed along the x -axis are also shown, defining the n_L , n_{cut} , and n'_{cut} quantities, respectively.

lowest-energy $L1_0$ configurations are dominated by the segregation of Co at the interface. This is because the Pt/MgO interaction, which is stronger than the Co/MgO one at low metal coordination (the number of first-neighbor metal atoms), drops abruptly with increasing coordination as Pt/Pt bonds compete with and quickly weaken the Pt/MgO ones, whereas this effect is much less pronounced for Co. Already at coordination number $Z = 4$, the Co/MgO interaction largely surpasses the Pt/MgO one. Co thus preferentially occupies interfacial sites as soon as their coordination is high enough to “quench” the Pt/MgO adhesion.¹² This interfacial effect in turn strongly reinforces the tendency of CoPt particles to $L1_0$ ordering:^{11,13,14} the presence of a Co first layer in fact favors the formation of a pure Pt second layer, and so on.

Even assuming an fcc-like $L1_0$ morphology, however, a thorough investigation at the first-principles level of supported particles with a number of atoms between, for example, 200 and 3000 is beyond available computational resources. To overcome this problem, we resort to a 1D modeling,¹⁵ that is, we focus on nanowires (1D systems) and take these as models of 0D nanoparticles with the same cross-section and aspect ratio. In Figure 1A–D, the correspondence between a truncated octahedral 0D cluster supported on a square-symmetry oxide surface to a 1D wire in which the section of the cluster is replicated ad infinitum is shown. Periodic symmetry is exploited to reduce the number of nonequivalent atoms in the unit cell used in the simulations (and also of the degrees of freedom of the system) and correspondingly the computational effort to a manageable size. Through the use of such models, 1D systems with a unit cell of 110–120 atoms can be constructed mimicking 0D particles

Table 1. Excess Energies E_{exc} (in eV) of Selected Suspended and Supported Nanowires^a

suspended wires	E_{exc}	supported wires	E_{exc}
$W_G(3,0)_{\text{Pt}}$	0.94	$W_S(3,0,1)$	1.04
$W_G(3,1)_{\text{Pt}}$	1.48	$W_S(3,0,2)$	1.30
$W_G(3,1)_{\text{Co}}$	1.05	$W_S(3,1,1)$	1.25
$W_G(4,0)_{\text{Pt}}$	0.93	$W_S(4,1,3)$	1.19
$W_G(4,1)_{\text{Pt}}$	0.86	$W_S(4,1,2)$	1.01
$W_G(4,1)_{\text{Co}}$	1.22		
$W_G(4,2)_{\text{Pt}}$	1.57		
$W_G(4,2)_{\text{Co}}$	1.01		
$W_G(5,1)_{\text{Pt}}$	1.03	$W_S(5,2,2)$	1.19
$W_G(5,2)_{\text{Pt}}$	0.75	$W_S(5,2,3)$	1.00
$W_G(5,2)_{\text{Co}}$	1.24	$W_S(5,2,4)$	1.26
$W_G(5,3)_{\text{Pt}}$	1.65		
$W_G(5,3)_{\text{Co}}$	0.97		
$W_G(6,1)_{\text{Pt}}$	0.68	$W_S(6,2,3)$	0.98
$W_G(6,3)_{\text{Pt}}$	0.67	$W_S(6,3,2)$	0.96
		$W_S(6,3,4)$	1.03
$W_G(7,0)_{\text{Pt}}$	0.63	$W_S(7,2,3)$	0.94
$W_G(7,2)_{\text{Pt}}$	0.56	$W_S(7,2,5)$	1.04
$W_G(8,1)_{\text{Pt}}$	0.54	$W_S(8,2,3)$	0.96
$W_G(8,3)_{\text{Pt}}$	0.46	$W_S(8,3,4)$	0.92
$W_G(9,2)_{\text{Pt}}$	0.37	$W_S(9,2,3)$	0.91
$W_G(9,4)_{\text{Pt}}$	0.38	$W_S(9,2,5)$	0.93
		$W_S(9,3,4)$	0.91

^a The wire nomenclature is explained in the text with the addition that the chemical element composing the largest layer of suspended wires is specified as a subscript (for supported wires this is always Pt).

with 7–8 times this number of atoms, which would otherwise be hardly affordable with present computational facilities. Except for very small particles, this has proven to be an effective tool to enlarge the scope of systems accessible to first-principles simulations.¹⁵

The lowest-energy wire configurations can then be constructed as follows. For suspended wires, starting from a rhomboidal (octahedral) section, fcc polyhedral sections are obtained by truncating the two outermost vertices, obtaining square (100) planes. A given wire is then characterized by two indexes: n_L , the length of one of the two diagonals of the rhombus (largest layer), and n_{cut} , the number of layers cut at each vertex, and will be denoted as $W_G(n_L, n_{\text{cut}})$ in the following, see Figure 1E. For supported wires, a further degree of freedom is given by the truncation at the interface: the number of layers cut in this case will be n'_{cut} and the corresponding wire will be denoted as $W_S(n_L, n_{\text{cut}}, n'_{\text{cut}})$, see Figure 1F.

For a proper comparison of the energetic stability of 1D systems, the excess energy per unit length (E_{exc}) or wire excess energy can be defined as¹⁶

$$E_{\text{exc}} = \frac{E_{\text{bnd}} - N_{\text{Pt}}E_{\text{Pt}} - N_{\text{Co}}E_{\text{Co}}}{\sqrt{N_{\text{tot}}}} \quad (1)$$

where N_{Pt} and N_{Co} are the number of Pt and Co atoms per unit length (section) of the wire, $N_{\text{tot}} = N_{\text{Pt}} + N_{\text{Co}}$, E_{Pt} , and E_{Co} are the bulk density functional (DF) total energies per atom of pure fcc Pt and hcp Co, respectively, and E_{bnd} is the wire binding energy per unit length, evaluated as the total energy of the

Table 2. Magnetic Moment per Co Atom (m_s) in Bohr Magnetons μ_B and Magnetic Anisotropy Energy per Co Atom (MAE) in meV of Optimal-Shape Suspended and Supported Nanowires (Nomenclature Detailed in the Text)

suspended wire	m_s	MAE	supported wire	m_s	MAE
$W_G(3,0)$	2.00	1.46	$W_S(3,0,1)$	1.88	3.22
$W_G(4,1)$	1.95	0.71	$W_S(4,1,2)$	1.86	4.31
$W_G(5,2)$	1.90	1.16	$W_S(5,2,3)$	1.85	2.41
$W_G(6,3)$	1.94	1.06	$W_S(6,3,2)$	1.85	2.14
$W_G(7,2)$	1.89	1.43	$W_S(7,2,3)$	1.85	1.25
$W_G(8,3)$	1.88	1.53	$W_S(8,3,4)$	1.84	0.90
$W_G(9,2)$	1.88	1.53	$W_S(9,3,4)$	1.85	0.82

wire/support combined system minus the energy of the MgO-(100) support in its equilibrium configuration. The most stable 1D structures correspond to the lowest values of the wire excess energy.

The energetics of selected free and supported nanowires are reported in Table 1. From an analysis of this table, in the gas-phase one observes a transition with increasing wire cross-section from optimal structures exhibiting no truncations [$W_G(3, 0)$] to one [$W_G(4, 1)$] and higher truncations. In particular, for $5 \leq n_L \leq 9$, structures with n_L odd and two truncations [$W_G(5, 2)$; $W_G(7, 2)$; $W_G(9, 2)$] alternate with structures n_L even and three truncations [$W_G(6, 3)$; $W_G(8, 3)$]. For supported wires, one correspondently observes a transition with increasing wire cross-section from structures exhibiting a single overhang [$W_S(3, 0, 1)$; $W_S(4, 1, 2)$; $W_S(5, 2, 3)$], to those exhibiting a triple [$W_S(6, 3, 2)$; $W_S(7, 2, 3)$; $W_S(8, 3, 4)$] and finally a quadruple or quintuple [$W_S(9, 3, 4)$] overhang. Some general rules can be derived. For free nanowires, the outmost (100) layers are always terminated with Pt atoms, which in agreement with experiment^{7,17} and results for 0D particles.^{11,12} A further preference is for wires with Pt on the largest layer, as it can also be drawn from an analysis of Table 1. The best gas-phase wires thus present odd $(4n + 1)$ magic numbers. For supported nanowires, the best truncations are found as a rule by combining the optimal suspended cuts with the simple rule: $n_{\text{cut}}' = n_{\text{cut}} + 1$. As discussed above, in fact, Co segregation replaces Pt segregation at the interface, entailing that the best supported arrangements are obtained by removing the outmost Pt layer in contact with the substrate. The best supported wires thus present even $(4n)$ magic numbers. The only exception to this rule is $W_G(6, 3)$ for which $W_S(6, 3, 2)$ is preferred over $W_S(6, 3, 4)$ [it can be noted that $W_S(6, 2, 3)$ is also very close in excess energy, suggesting that at this size a transition among different morphologies occurs]. This is in tune with the Wulff (for free particles) or Wulff–Kaishev (for supported particles) construction,⁶ that is, the optimal shape predicted by proportioning the truncations to the surface¹⁸ and interface (or adhesion)¹² energies. In passing, it can be observed that the mismatch of the wire and substrate lattice parameters induces the development of interfacial dislocations¹⁹ (not shown).

Once the lowest-energy structures have been ascertained, their magnetic properties can be investigated. We recall that in the bulk CoPt alloys at 1:1 composition exhibit a $L1_0$ structure with an a axis of 3.793 Å and a c/a ratio of 0.969,²⁰ while the MAE is 0.8 meV per Co atom.² Our DF approach reasonably reproduces the structural features: the predicted values are 3.829 Å and 0.979 for the a axis and c/a ratio, respectively. The MAE instead is

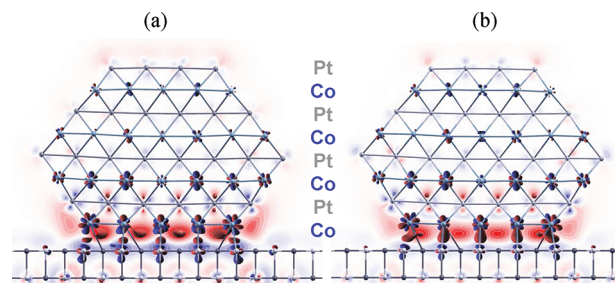


Figure 2. Isocontours of differential electronic density $\Delta\rho = \rho(\text{CoPt/MgO}) - \rho(\text{CoPt}) - \rho(\text{MgO})$, obtained by subtracting the electron density of the MgO(surface) and CoPt(wire) from the total electron density of the $W_S(8,3,4)$ wire. The total density (a) or the minority spin density (b) are shown. The view is taken along the main axis of the wire. Positive values of $\Delta\rho$ (corresponding to an increase in density) are in red. Contour value = 0.004 e/Å³. Planes of cobalt atoms are displayed in blue, platinum atoms are displayed in dark gray.

1.76 meV per Co atom, that is, it is substantially overestimated. However, we underline that our focus here is on the qualitative trends and features of the effects of the metal/oxide interface on the magnetism of supported nanostructures, which should be correctly singled out by our first-principles approach.

In Table 2, the values of the magnetic moments and the MAE of selected suspended and supported CoPt nanowires are shown. Three main conclusions can be drawn from an analysis of this table. (i) Both free and deposited systems present large magnetic moments; their average values on the Co atoms range around $m_s = 1.9/2.0 \mu_B$, and are roughly comparable with the bulk value of $m_s = 1.96 \mu_B$. However, the values for the deposited systems are somewhat smaller than the gas phase, and this decrease is essentially due to the Co atoms at the interface with the MgO-(100) surface which present average m_s values around 1.78/1.80 μ_B . This is already an indication that the particle/oxide interface do play a significant role. (ii) The most stable orientation of the easy-axis of magnetization turns out to be perpendicular to the surface, thus satisfying one of the two main requests for nanospintronics. Note that we did not include in our analysis dipolar interactions among the particles that could also stabilize this magnetization orientation.²¹ The second most stable orientation is invariably the one orthogonal to the wire and parallel to the surface. (iii) While the MAE of the free nanowires approaches the DF-predicted bulk value (1.76 meV/Co-atom) with increasing size, the deposited nanowires converge in this size interval to a value which is roughly one-half of the bulk one. This is not a peculiarity of our 1D modeling. The comparison of the MAE of 1D and 0D systems in fact turns out to be reasonable; for example, a $W_S(5, 2, 3)$ nanowire has a MAE per Co atom of 2.4 meV to be compared with 1.4 meV for the corresponding 62 atom $\text{Co}_{32}\text{Pt}_{30}$ cluster (see the top of Figure 1). The agreement between the two systems is thus already fair for small systems and is expected to become more and more accurate with increasing size (also the geometrical parameters of the interlayer distances and interfacial deformation, not shown, compare favorably). Moreover, this prediction is in tune with available experimental data.²² The metal/oxide interface is therefore crucial in determining the magnetism of supported CoPt nanostructures and their possible use in applications.

Let us rationalize these findings. In Figure 2, plots of differential electron density due to the adsorption of a CoPt wire onto the MgO(100) support are shown. As clearly evidenced from

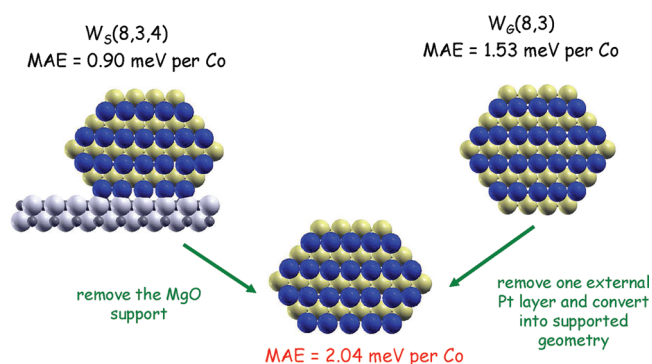


Figure 3. Interface effects on the MAE of CoPt nanostructures.

these plots, a charge transfer from the MgO surface to the CoPt clusters occurs. This is consistent with analogous charge transfer effects that have been described, for example, when MgO slabs are deposited on Ag(100), causing a substantial decrease of the system work function.²³ In the present context, the transferred electrons populate the partially vacant d-orbitals of the Co atoms, in particular the minority spin orbitals, as apparent from a comparison of Figure 2 panel a and panel b, thus explaining the decrease of their magnetic moments in Table 1. In view of tuning interface effects, it should be noted that other oxides with different work function can behave differently, and possibly produce inverse charge transfer effects (a possibility currently under study in our group). The analysis of the MAE is more subtle. First, we checked that the charge transfer from the MgO surface to the CoPt cluster is of similar entity for both directions of the magnetization axis, so that it cannot account for the reduction in the MAE. Second, this reduction is neither due to a geometric (structural reconstruction) effect. On the opposite, the structural relaxation especially of the interface Co layer with the development of interfacial dislocations is beneficial to increase the MAE of the system. In Figure 3, we indeed show that by removing the MgO surface keeping the CoPt configuration frozen and evaluating the MAE of such a hypothetical gas-phase system one finds a large increase in the value of the MAE, which turns out to be even larger than that of the corresponding optimal CoPt nanowire. The MAE reduction thus has a different origin. In Figure 4, plots of differential electron density $\Delta\rho$ due to the switching of the magnetization axis from parallel to perpendicular to the surface are shown for both suspended and supported nanowires. A critical inspection of these plots shows first of all that this switching induces a charge flow into the Co and Pt(100) planes (positive value of $\Delta\rho$). For the unsupported wire this charge flow occurs especially in the external or contour atoms while it is much reduced in the interior of the wire. Deposition onto the surface appreciably increases this charge flow as demonstrated by the increase of the regions where $\Delta\rho$ is large. This behavior can be rationalized. We recall that the energetics of magnetization essentially depend on the residual orbital momentum as the spin momentum “follows” the orbital one for energetic reasons due to the LS spin–orbit term in the Hamiltonian. The inspection of Figure 4 crucially shows that switching the magnetization axis leads to occupying states that are extended in the (100) planes of the wire. The value of the MAE mainly depends on which type of d-states are available at the Fermi energy. The substantial increase of the regions where $\Delta\rho$ is large in Figure 4b with respect to Figure 4a indicates that in

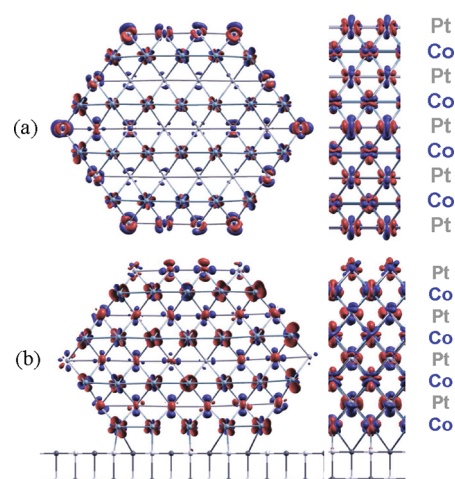


Figure 4. Isocontours of differential electronic density $\Delta\rho = \rho(M_z) - \rho(M_y)$, obtained by subtracting the total electron density of the state in which the magnetization axis is parallel to the surface and perpendicular to the wire main axis (M_y) from the state in which the magnetization axis is perpendicular to the surface (M_z), for the suspended $W_6(8,3)$ (a) or supported $W_5(8,3,4)$ (b) wires. In the larger images on the left, the view is taken along the main axis of the wire; on the right side view of the wire is also shown. Contour value = $0.004 \text{ e}/\text{\AA}^3$. Color coding as in Figure 2.

the supported system both in- and out-of-plane d-states are available at the Fermi energy. This availability results in a reduction of the energy cost associated with magnetization switching and thus a reduction of the MAE. Note that it is not possible to associate this reduction with selective spin–orbit induced splittings at the Fermi surface as hypothesized for other systems.²⁴

From the previous analysis we can then summarize the three main factors which determine the magnetism of supported nanoparticles: (a) chemical ordering: preferential metal/substrate interactions can lead to interfacial enrichment of one element; (b) epitaxy: the need to accommodate to the substrate can induce structural relaxations (prodrums of dislocations); (c) electronic structure: the mixing of the particle and support electronic states, with a possible charge transfer from/to the support and more subtle effects connected with spin–orbit coupling.

In the case of CoPt nanoparticles on MgO(100), point (a) leads to a major feature, that is, one-layer segregation of the magnetic element (Co) at the interface, due to many-body effects in the metal/surface interaction. As cubic structures are favored on checkerboard/square-symmetry surface for sufficiently large sizes, this also implies (point b) a stabilization of the $L1_0$ arrangement with respect to noncrystalline motifs, a magnetization easy axis perpendicular to the surface (thus satisfying one of the two main requirements of nanospintronics) and an interfacial deformation due to epitaxial effects that is beneficial to increase the MAE. This last effect is however overwhelmed by the mixing of particle and oxide electronic wave functions at the interface (point c) that dominates and results in a decrease of the magnetic moments at the interface and eventually to a reduction of the MAE by a factor $\sim 1/2$. For medium-sized particles of interest for nanospintronics, interface effects thus play a crucial role not only on the magnitude and orientation of the particle magnetic moments, but especially on their MAE. Apart from rationalizing the observed behavior in a specific case, a full understanding of these factors can be helpful in the design and fine-tuning of the magnetism of supported nanoparticles. By modulating the

mixing of electronic states at the interface via a change in the oxide support it may be possible to increase the MAE and achieve systems of use in room-temperature magnetic recording.

Methods. Total energy calculations within a DF approach are performed using periodic boundary conditions,²⁵ a gradient-corrected²⁶ XC-functional, and ultrasoft pseudopotentials.²⁷ In the modeling of 1D periodic systems, orthorhombic unit cells are employed, extending 2.9755 Å (corresponding to the distance between first-neighbor oxygen atoms on the MgO(100) surface) along the periodicity (x) direction and extending in the other two directions (y and z) in such a way that the distance between atoms belonging to replicated cells is at least 8–10 Å in order to reduce spurious interactions. The MgO(100) oxide surface is modeled by a three-layer slab with the first two layers free to relax and the bottom one frozen at the experimental lattice parameter, having verified that this model is converged with respect to the number of layers. In particular, calculations with five MgO layers (the first three frozen) on the $W_S(8, 3, 4)$ wire produced results essentially identical to those obtained using only three layers. In the optimization of the wires structure, we use numerical parameters similar to those employed in ref 12: 30 Ryd for the energy cutoff for the selection of the plane wave basis set for describing the wave function and 150 Ry for describing the electronic density (1 Ryd = 13.606 eV). The sampling of the first Brillouin zone is performed using a (4,1,1) mesh of k points, where the denser sampling corresponds to the wires periodicity direction. All the calculations are performed spin unrestricted. Relativistic contributions are evaluated by adding a noncollinear spin–orbit term to the scalar-relativistic approximation within a local density approximation framework, as this choice of the XC-functional does not seem to worsen the estimation of the MAE with respect to an estimation using a generalized gradient approximation approach (computationally more demanding).²⁸ A Lowdin projection analysis of the wave function furnishes the contribution of individual atoms to the magnetic moment of the system, while the magneto-crystalline contribution to the MAE is calculated by subtracting total energies between configurations with different orientation of the magnetization axis. In the evaluation of the MAE, we increase the numerical accuracy of the DF calculations by performing single-point DF energy evaluations by choosing 40 and 400 Ry as the energy cutoffs for the wave functions and the electronic density, respectively.

The search for the lowest-energy structures of CoPt supported nanoparticles follows the lines of our previous work.¹² In a first step, a many-body empirical potential for the metal–metal interactions and a surface energy empirical potential fitted to DF calculations for the metal-oxide ones¹² is used to perform a systematic sampling. Candidate structures for DF optimization are then taken as the low-energy configurations of each structural motif from this search at 50–50% composition but also translating those obtained at different compositions by optimizing the chemical ordering via an exchange-only approach, or as configurations built via the Wulff-Kaishev construction⁶ with $L1_0$ chemical ordering. System comparison techniques are so utilized to maximize structural diversity and the thoroughness of the search. The final structures on which the MAE is calculated are thus grounded on a first-principles basis.

AUTHOR INFORMATION

Corresponding Author

*E-mail: alessandro.fortunelli@cnr.it.

ACKNOWLEDGMENT

A.F. is grateful to Paola Luches and Sergio Valeri for enlightening discussions, Livia Giordano for useful validation tests, Alberto Coduti for technical assistance, and gratefully acknowledges financial support from the SEPON project within the Advanced Grants of the European Research Council. The DF calculations have been performed at the Cineca Supercomputing Center (Bologna, Italy) within an agreement with Italian CNR. Networking via the MP0903 COST Action is also acknowledged.

REFERENCES

- (1) Bernard-Mantel, A.; Seneor, P.; Bouzehouane, K.; Fusil, S.; Deranlot, C.; Petroff, F.; Fert, A. *Nat. Phys.* **2009**, *5*, 920–924.
- (2) Weller, D.; Moser, A. *IEEE Trans. Magn.* **1999**, *35*, 4423–4439.
- (3) Chappert, C.; Fert, A.; Nguyen Van Dau, F. *Nat. Mater.* **2007**, *6*, 813.
- (4) Bansmann, J.; Baker, S. H.; Binns, C.; Blackman, J. A.; Bucher, J.-P.; Dorantes-Dávila, J.; Dupuis, V.; Favre, L.; Kechrakos, D.; Kleibert, A.; Meiwe-Broer, K.-H.; Pastor, G. M.; Perez, A.; Toulemonde, O.; Trohidou, K. N.; Tuillon, J.; Xie, Y. *Surf. Sci. Rep.* **2005**, *56*, 189–275.
- (5) Lehnert, A.; Dennler, S.; Blonski, P.; Rusponi, S.; Etzkorn, M.; Moulas, G.; Bencok, P.; Gambardella, P.; Brune, H.; Hafner, J. *Phys. Rev. B* **2010**, *82*, 094409.
- (6) Henry, C. R. *Prog. Surf. Sci.* **2005**, *80*, 92–116.
- (7) Favre, L.; Dupuis, V.; Bernstein, E.; Melinon, P.; Perez, A.; Stanesco, S.; Simon, J. P.; Babonneau, D.; Tonnerre, J. M.; Hodeau, J. L. *Phys. Rev. B* **2006**, *74*, 014439.
- (8) Gauthier, Y.; Schmid, M.; Padovani, S.; Lundgren, E.; Bus, V.; Kresse, G.; Redinger, J.; Varga, P. *Phys. Rev. Lett.* **2001**, *87*, 036103.
- (9) Ferrando, R.; Rossi, G.; Nita, F.; Barcaro, G.; Fortunelli, A. *ACS Nano* **2008**, *2*, 1849–1856.
- (10) Penuelas, J.; Andreazza, P.; Andreazza-Vignolle, C.; Tolentino, H. C. N.; De Santis, M.; Mottet, C. *Phys. Rev. Lett.* **2008**, *100*, 115502.
- (11) Rollmann, G.; Gruner, M. E.; Hucht, A.; Meyer, R.; Entel, P.; Tiago, M. L.; Chelikowsky, J. R. *Phys. Rev. Lett.* **2007**, *99*, 083402.
- (12) Barcaro, G.; Ferrando, R.; Fortunelli, A.; Rossi, G. *J. Phys. Chem. Lett.* **2010**, *1*, 111–115.
- (13) Sato, K. *Nat. Mat.* **2009**, *8*, 924.
- (14) Alloyeau, D.; Ricolleau, C.; Mottet, C.; Oikawa, T.; Langlois, C.; Le Bouar, Y.; Braidry, N.; Loiseau, A. *Nat. Mat.* **2009**, *8*, 940.
- (15) Molina, L. M.; Hammer, B. *Phys. Rev. B* **2004**, *69*, 155424.
- (16) Tommei, G. E.; Baletto, F.; Ferrando, R.; Spadacini, R.; Danani, A. *Phys. Rev. B* **2004**, *69*, 115426.
- (17) Shapiro, A. I.; Rooney, P. W.; Tran, M. Q.; Hellman, F.; Ring, K. M.; Kavanagh, K. L.; Rellinghauss, B.; Weller, D. *Phys. Rev. B* **1999**, *60*, 12826.
- (18) Dannenberg, A.; Gruner, M. E.; Hucht, A.; Entel, P. *Phys. Rev. B* **2009**, *80*, 245438.
- (19) Freund, L. B.; Suresh, S. *Thin Film Materials: stress, defect formation surface evolution*; Cambridge University Press: Cambridge, 2003.
- (20) Hultgren, R.; Desai, P. D.; Hawkins, D. T.; Gleiser, M.; Kelley, K. K. *Values of the thermodynamic properties of binary alloys*; American Society for Metals; Jossey-Bass Publishers: Materials Park, Ohio, United States, 1981.
- (21) Chantrell, R. W.; Walmsley, N.; Gore, J.; Maylin, M. *Phys. Rev. B* **2000**, *63*, 024410.
- (22) Ersen, O.; Parasote, V.; Pierron-Bohnes, V.; Cadeville, M. C.; Ulhaq-Bouillet, C. *J. Appl. Phys.* **2003**, *93*, 2987.
- (23) Prada, S.; Martinez, U.; Pacchioni, G. *Phys. Rev. B* **2008**, *78*, 235423.
- (24) Sipr, O.; Bornemann, S.; Minár, J.; Ebert, H. *Phys. Rev. B* **2010**, *82*, 174414.
- (25) Giannozzi, P.; Baroni, S.; Bonini, N.; Calandra, M.; Car, R.; Cavazzoni, C.; Ceresoli, D.; Chiarotti, G. L.; Cococcioni, M.; Dabo, I.; Dal Corso, A.; de Gironcoli, S.; Fabris, S.; Gebauer, R.; Gerstmann, U.; Fratesi, G.; Gougoussis, C.; Kokalj, A.; Lazzeri, M.; Martin-Samos, L.; Marzari, N.; Mauri, F.; Mazzarello, R.; Paolini, S.; Pasquarello, A.

Paulatto, L.; Sbraccia, C.; Scandolo, S.; Sclauzero, G.; Seitsonen, A. P.; Smogunov, A.; Umari, P.; Wentzcovitch, R. M. *J. Phys.: Condens. Matter* **2009**, *21*, 395502.

(26) Perdew, J. P.; Burke, K.; Ernzerhof, M. *Phys. Rev. Lett.* **1996**, *77*, 3865–3868.

(27) Vanderbilt, D. *Phys. Rev. B* **1990**, *41*, 7892–7895.

(28) Baroni, S.; Mosca Conte, A.; Fabris, S. *Phys. Rev. B* **2008**, *78*, 014416.